PHYSICAL REVIEW A **89**, 023432 (2014)

Imaging the impulsive alignment of noble-gas dimers via Coulomb explosion

A. von Veltheim, B. Borchers, G. Steinmeyer, and H. Rottke*

Max-Born-Institut für Nichtlineare Optik und Kurzzeitspektroskopie, Max-Born-Straße 2A, D-12489 Berlin, Germany

(Received 18 December 2013; published 28 February 2014)

The impulsive alignment of the noble-gas dimers Ne_2, Ar_2, Kr_2, and Xe_2 is experimentally investigated by determining the alignment through Coulomb explosion imaging after their double ionization. This approach yields a favorably detailed insight into the temporal evolution of the alignment succeeding the aligning laser pulse. Particular emphasis is put on analyzing higher order coherences induced in the density matrix as these coherences determine the details of the temporal evolution of the aligned molecular ensemble. The recorded data enable an extraction of polarizability anisotropies for the dimers and of their rotational constants in the vibrational ground state. At the elevated level of rotational excitation obtained, centrifugal distortion starts influencing the temporal evolution of the alignment.

DOI: 10.1103/PhysRevA.89.023432 PACS number(s): 33.80.Rv, 33.80.Wz, 32.80.Rm, 33.20.Xx

I. INTRODUCTION

Extensive work has been devoted to the theoretical and experimental study of laser-induced molecular alignment by short, intense laser pulses (for a review, see [1,2]). Laser-induced alignment occurs when a laser pulse interacts with a molecule via its polarizability, either adiabatically [3] or impulsively [4]. If the laser pulse is short compared to the rotational time scale of the molecule, a broad, coherent superposition of rotational eigenstates is excited via Raman-type transitions [4]. The coherence gives rise to a sharp localization of the molecular axis in angular space, appearing shortly after the laser pulse. As long as coherence within this rotational wave packet is preserved, the wave packet dephases and revives periodically at well-defined instants of time. The revivals are accompanied by a realignment of the molecular axis. Therefore, a nonadiabatic alignment of molecules enables studying the alignment dependence of various processes under external-field-free conditions, including, for example, photoionization [5,6], high-harmonic generation [7–9], and chemical reactions [10]. This approach essentially allows the realization of experiments in a molecule-fixed frame of reference. On the other hand, it is these very processes that can be employed for characterization or optimization of the alignment and to study the rotational dynamics of a molecule by itself [11]. Experimentally, the most detailed insight into the temporal evolution of the rotational wave packet can usually be gained by dissociating the molecule and by detecting the angular distribution of the fragments, provided that the time scale for dissociation is short compared to molecular rotation; see, e.g., [12,13].

Here we investigate the rotational motion of noble-gas dimers after impulsive alignment by a laser pulse. These molecules have very small rotational constants, implying a long rotational period in a time range large compared to 1 ps. The slow rotation allows applying laser pulses with picosecond widths for the creation of an alignment while still being well in the nonadiabatic regime of alignment. Together with the high ionization potentials of the dimers, it is therefore possible to expose the dimers to a high laser pulse fluence, yet without significant electronic excitation or even ionization. Consequently, starting with a molecular ensemble cooled to a low temperature, we are able to excite a rotational wave packet that comprises a wide span of rotational states up to a rotational quantum number $J \approx 20$, which is significantly wider than the initial thermal distribution. At such elevated excitation levels, two aspects start to play a significant role in the dynamical evolution of the wave packet. First, the fact that noble-gas dimers are nonrigid rotors starts to influence the wave packet dynamics on longer time intervals. Second, the high laser pulse fluence inevitably leads to a significant redistribution of the rotational population, inducing coherences between rotational states with considerably different rotational quantum numbers J that cannot be coupled by a single Raman transition.

The temporal evolution of the ensemble average of $\cos^2\theta$ is usually investigated in experiments on laser-induced impulsive alignment. Here, θ represents the polar angle between the internuclear axis and the direction of polarization of the aligning laser beam. While this quantity can certainly reliably characterize the net alignment of the molecular ensemble, it falls short of a complete characterization of the coherences present in the rotational motion that was induced by the laser pulse [11,13,14]. To this end, we therefore investigate the evolution of rotational wave packets via Coulomb explosion imaging, using an ultrashort high-intensity laser pulse which doubly ionizes the dimer. This approach opens the most concise access possible to the temporal evolution of the wave packet. As Coulomb explosion proceeds rapidly compared to molecular rotation, the angular distribution of the ions represents a snapshot of the molecular axis alignment at the incident of ionization. From recordings of these angular distributions it therefore is possible, in principle, to extract all higher order coherences induced in the rotational motion of the dimer [11]. It needs to be emphasized that these coherences are not easily accessible using other methods, e.g., Raman-induced polarization spectroscopy and high-order harmonic or angularly resolved photoelectron spectroscopy [11]. In the following, we show that higher order coherences are indeed present in the rotational wave packet induced by the aligning pulse. We measure coherences between rotational states that have a spacing up to $\Delta J = 8$, i.e., requiring at least four successive rotational Raman transitions. Finally, rotational constants and estimates for the polarizability anisotropies of

*rottke@mbi-berlin.de

Ne_2, Ar_2, Kr_2, and Xe_2 are extracted from our experimental data.

Experimental investigations on the alignment of noble-gas dimers were first reported by Minemoto *et al.* [15,16], using long laser pulses to adiabatically align the molecules. From these measurements the anisotropy of the polarizability of Ar_2, Kr_2, and Xe_2 was deduced. It is this anisotropy that is responsible for the possibility to align a molecule by an applied electric field. Moreover, Wu *et al.* [17] investigated the impulsive, nonadiabatic alignment of Ar_2 by tracking the temporal evolution of the wave packet formed after the aligning laser pulse by Coulomb exploding the dimer, which is widely similar to our approach discussed below.

II. THEORETICAL BACKGROUND

In this section, we introduce the basic theoretical tools that we employ to analyze and interpret our experimental data. Alignment of the noble-gas dimers is accomplished by an intense laser pulse that exhibits a short temporal width compared to the respective dimer period of rotation. This precondition locates us in the impulsive regime of molecular alignment [4,11,18]. Prior to application of the aligning laser pulse, we start with a thermal ensemble of dimers, the rotational distribution of which is characterized by a certain rotational temperature T. We assume that the dimers are in their vibrational ground state, which is a reasonable assumption at the low temperatures in the supersonic gas jet used in our experiment. The aligning laser pulse efficiently drives rotational Raman transitions, which are responsible for the alignment within the sample. Vibrational Raman transitions are, however, negligible at the light intensities used here as the corresponding transition matrix elements are at least a factor of ten smaller than those for rotational Raman transitions (for Ar_2, see, e.g., [19,20]).

Based on these facts and given that the alignment pulse is far off resonance of any dipole allowed transition in the investigated dimers, the Hamiltonian that governs the evolution in time of the molecular rotation reads [3]

$$H(t) = H_{\mathrm{rot}} - \tfrac{1}{4}E_0^2(t)\Delta\alpha\cos^2\theta, \tag{1}$$

with $E_0(t)$ being the pulse envelope of the electric field of the aligning laser pulse, θ the polar angle of the dimer axis with respect to the electric field vector of the laser pulse (which is assumed to be linearly polarized), and $\Delta\alpha = \alpha_\parallel - \alpha_\perp$ the difference between the polarizabilities of the dimer parallel ($\alpha_\parallel$) and perpendicular ($\alpha_\perp$) to the internuclear axis. H_{rot} is the Hamiltonian of free rotation for a diatomic molecule, which we will approximate by

$$H_{\mathrm{rot}} = B\boldsymbol{J}^2 - D\boldsymbol{J}^4, \tag{2}$$

with the second term including the possibility of centrifugal distortion to lowest order. B and D are the corresponding rotational constants and $\boldsymbol{J}$ the angular momentum operator.

For the time frame of the aligning laser pulse, i.e., the time interval from $t = 0$ to τ, we numerically integrate the Schrödinger equation for the time evolution operator $U(t,0)$ that we refer to as propagator in the following:

$$i\frac{\partial U(t,0)}{\partial t} = \left[H_{\mathrm{rot}} - \frac{1}{4}E_0^2(t)\Delta\alpha\cos^2\theta\right]U(t,0). \tag{3}$$

As we are interested in the temporal evolution of the dimer's rotational motion after the aligning laser pulse, we have to determine the propagator for $t > \tau$. In this time interval $U(t,\tau)$ assumes the simple form:

$$U(t,\tau) = \exp[-i(t-\tau)H_{\mathrm{rot}}],\ t > \tau. \tag{4}$$

The overall propagator for the rotational motion at times $t > \tau$, starting at $t = 0$, is then given by

$$\begin{aligned} U(t,0) &= U(t,\tau)U(\tau,0) \\ &= \exp[-i(t-\tau)H_{\mathrm{rot}}]U(\tau,0). \end{aligned} \tag{5}$$

We may characterize the overall effect of the impulsive aligning laser pulse on the rotation by a single, dimensionless parameter a that we refer to as "kick" parameter in the following:

$$a = \frac{\Delta\alpha}{4}\int_0^\tau dt\ E_0^2(t). \tag{6}$$

The detailed shape of the laser pulse $E_0(t)$ has only a minor effect on the alignment of the dimer achieved at the end of the pulse.

At time $t = 0$ the ensemble of dimers is statistically distributed over the dimer rotational states, corresponding to a specific temperature T. Moreover, we assume that the dimers are originally in the vibrational and electronic ground states. This ensemble is described by a density operator ρ_0. Its matrix representation, based on the rotational eigenstates of H_{rot} [i.e., the spherical harmonics $Y_{JM}(\theta,\varphi)$ in our case], is given by

$$\rho_{0\,J,M;J',M'} = g_J\frac{\exp(-E_J/kT)}{Z(T)}\delta_{M,M'}\delta_{J,J'}. \tag{7}$$

Here

$$Z(T) = \sum_J g_J(2J+1)\exp(-E_J/kT)$$

is the sum over states, g_J the statistical weight of the respective rotational state, and E_J the corresponding eigenvalue of H_{rot}. M is the magnetic quantum number with respect to a suitably chosen and spatially fixed coordinate axis. Here we use the direction of polarization of the aligning laser pulse. The evolution in time of this initial density operator is then ruled by the propagator given in Eq. (5) via

$$\rho(t) = U(t,0)\rho_0 U^\dagger(t,0). \tag{8}$$

From $\rho(t)$ we can determine the observable of our experiment, namely $\tilde{\rho}(\theta,\varphi,t)$, i.e., the probability density to find the internuclear axis aligned with the direction (θ,φ) according to

$$\tilde{\rho}(\theta,\varphi,t) = \frac{\partial^2}{\partial\theta\,\partial\varphi}\mathrm{Tr}\left[\rho(t)\frac{P_{\theta,\varphi}}{\sin\theta}\right].$$

Here Tr is the trace operator and $P_{\theta,\varphi}$ a projection operator acting on functions f defined on the unit sphere via

$$P_{\theta,\varphi}f(\theta',\varphi') = \begin{cases} f(\theta',\varphi'), & 0 \leqslant \theta' \leqslant \theta \quad \text{and} \quad 0 \leqslant \varphi' \leqslant \varphi, \\ 0, & \text{elsewhere.} \end{cases}$$

Employing spherical harmonics as a basis set, we then arrive at the expression

$$\tilde{\rho}(\theta,\varphi,t) = \sum_{J,J',M} \rho_{J,M;J',M}(t) Y^*_{J',M}(\theta,\varphi) Y_{J,M}(\theta,\varphi), \quad (9)$$

for $\tilde{\rho}(\theta,\varphi,t)$. This result widely agrees with the formalism developed in [11]. $\rho_{J,M;J',M}(t) = \langle J,M|\rho(t)|J',M\rangle$ are the matrix elements of the density operator with respect to the spherical harmonics. ρ_0 [Eq. (7)] and the propagator [Eq. (5)] yield nonvanishing matrix elements of ρ only for equal M for the bra and the ket. This, in turn, implies that $\tilde{\rho}(\theta,\varphi,t)$ is actually independent of the azimuthal angle φ [$\tilde{\rho} = \tilde{\rho}(\theta,t)$; see Eq. (9)]. More explicitly, the matrix elements of the density operator are given by

$$\begin{aligned}\rho_{J,M;J',M}(t) &= \exp[i(E_J - E_{J'})(t-\tau)] \\ &\times \sum_{J''} \frac{g_{J''}\exp(-E_{J''}/kT)}{Z(T)} \\ &\times \langle J',M|U(\tau,0)|J'',M\rangle\langle J,M|U(\tau,0)|J'',M\rangle^*. \quad (10)\end{aligned}$$

In the extreme impulsive limit $\tau \to 0$, the term $U(\tau,0)$ has the simple analytic form

$$U(\tau,0) = \exp(ia\cos^2\theta),$$

and shows explicitly the independence of the alignment of the specific shape of the laser pulse. Here a is the "kick" parameter specified in Eq. (6).

$\tilde{\rho}(\theta,\varphi,t)$ can be used for the calculation of the expectation value over the ensemble of molecules after the alignment laser pulse for any given function $f(\theta,\varphi)$ [11]; i.e.,

$$\langle f\rangle(t) = \mathrm{Tr}[\rho(t)f] = \int d\mathbf{\Omega}\, \tilde{\rho}(\theta,\varphi,t) f(\theta,\varphi), \quad (11)$$

where $\mathbf{\Omega}$ is the solid angle determined by θ and φ. Specifically, Eq. (11) can be used to calculate $\langle\cos^2\theta\rangle$, i.e., the standard quantity employed to characterize the alignment of a molecular ensemble. Moreover, the higher moments $\langle\cos^{2n}\theta\rangle$ with $n > 1$ may also be evaluated to the end of providing more detailed information on the coherence induced in the rotation of a molecular ensemble by the aligning laser pulse. A full reconstruction of the information contained in $\tilde{\rho}(\theta,\varphi,t)$ is only possible if all $\langle\cos^{2n}\theta\rangle$ with $n \geqslant 1$ are known. If experimentally applicable, Coulomb explosion imaging enables direct access to $\tilde{\rho}(\theta,\varphi,t)$. Our method therefore provides the most detailed information on the alignment of a molecular ensemble, without necessitating any detour via experimental determination of the $\langle\cos^{2n}\theta\rangle$ [11,13].

Choosing values for parameters a and T as they are typical in the below-reported alignment experiments for the Ar_2 dimer, we show the calculated temporal evolution of $\tilde{\rho}(\theta,t)$ [Eq. (9)] in Fig. 1 after an impulsive alignment laser pulse. For clarity, the end of the laser pulse has been chosen as the origin $t = 0$ of the time axis in this plot, and the duration has been chosen to include one full revival of the alignment. We used the following rotational constants for Ar_2 in the calculations: $B_0 = 0.0576\ \mathrm{cm}^{-1}$ and $D_0 = 1.2 \times 10^{-6}\ \mathrm{cm}^{-1}$, respectively. These values are close to those given in [21]. Given the below experimental conditions, we assume exclusive

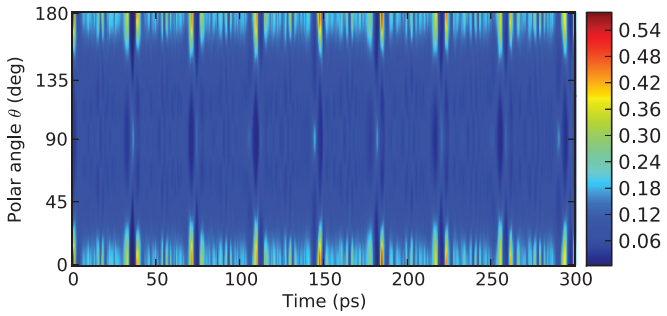

FIG. 1. (Color online) Temporal evolution of the probability density $\tilde{\rho}(\theta,t)$ [Eq. (9)] to find the internuclear axis of Ar_2 dimers aligned with an angle θ relative to the direction of polarization of an aligning laser pulse after the pulse passed. Pulse parameters are width, 1.4 ps (FWHM); kick parameter, $a = 11.0$ [Eq. (6)]; $\sin^2$ pulse shape. The time interval has been selected to include the first full revival of the alignment at $T_{\mathrm{rev}} = 289.5$ ps. The temperature of the initial distribution over rotational states in the molecular ensemble was assumed as 2.5 K.

population of the vibrational dimer ground state. The vector of linear polarization of the laser pulse is aligned with the z axis ($\theta = 0$ in Fig. 1). As can be seen in Fig. 1, $\tilde{\rho}(\theta,t)$ shows a very intricate structure. For a quantitative view of the alignment of the dimer sample, Fig. 2 shows a cut through $\tilde{\rho}(\theta,t)$ at $t = 218.0$ ps. Two cuts at fixed polar angles $\theta = 0°$ and $54°$ in Fig. 3 show the temporal evolution of the probability density quantitatively. The instant of time for the cut at fixed delay relative to the aligning laser pulse (Fig. 2) was suitably chosen to display the angular distribution of the internuclear axis of the dimer ensemble for the maximum achievable alignment. In our case, this condition is reached at $t = 3T_{\mathrm{rev}}/4$ with $T_{\mathrm{rev}} = 1/2B_0c$ being the full revival period of the alignment [12] and c the speed of light. For Ar_2 T_{rev} amounts to 289.5 ps. At this particular instant, a very pronounced alignment of the internuclear axis of the Ar_2 dimers appears in the direction of the laser pulse polarization axis.

Similar to all noble-gas isotopes with even mass numbers, the Ar atom has zero nuclear spin. This fact is responsible for

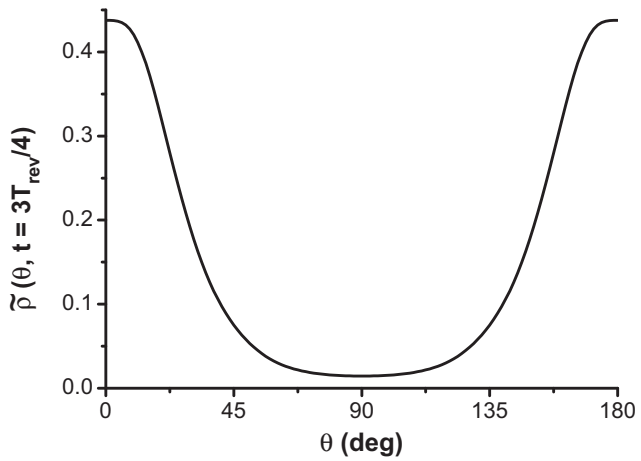

FIG. 2. Cut through Fig. 1 at the time $t = 3T_{\mathrm{rev}}/4 = 218.0$ ps where the highest possible alignment of Ar_2 is found.

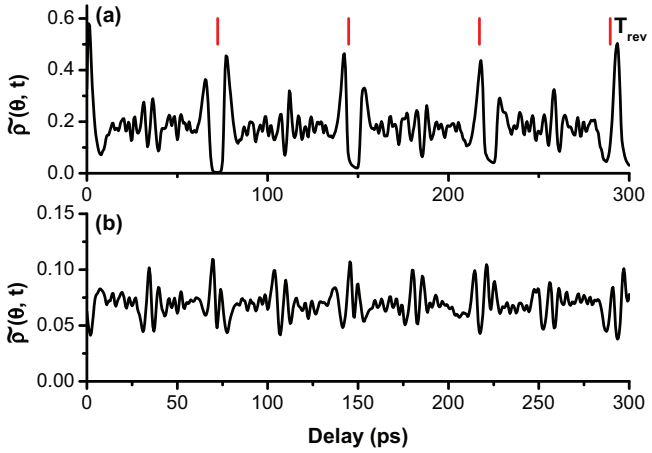

FIG. 3. (Color online) Cuts through Fig. 1 in the direction of the time axis at angles (a) $\theta = 0^\circ$ and (b) 54°. The markers indicate the fractional revivals of the alignment of Ar_2 at times $nT_{rev}/4$ with $n = 1,2,3,4$.

vanishing statistical weights g_J in the relation for the initial density matrix [Eq. (7)] for all odd angular momenta J. For all even J the g_J equal unity. In turn, this simple structure of the g_J has considerable influence on the revival structure of the alignment as it generates fractional revivals at times $nT_{rev}/4$ with $n = 1,2,...$; see, e.g., [17]. These particular revivals are marked in Fig. 3 by vertical markers. While there are clear signatures of the partial fractional revivals at $\theta = 0^\circ$, their visibility becomes less pronounced at larger values of θ; see, e.g., Fig. 3(b), which shows the case $\theta = 54^\circ$.

Figure 4 shows the temporal evolution of the two lowest order expectation values of $\cos^{2n}\theta$ [Eq. (11)] up to $2T_{rev}$ for the Ar_2 example ($n = 1,2$). Here $\langle\cos^2\theta\rangle(t)$ is shown as a blue dashed line. Partial revival structures of the dimer alignment

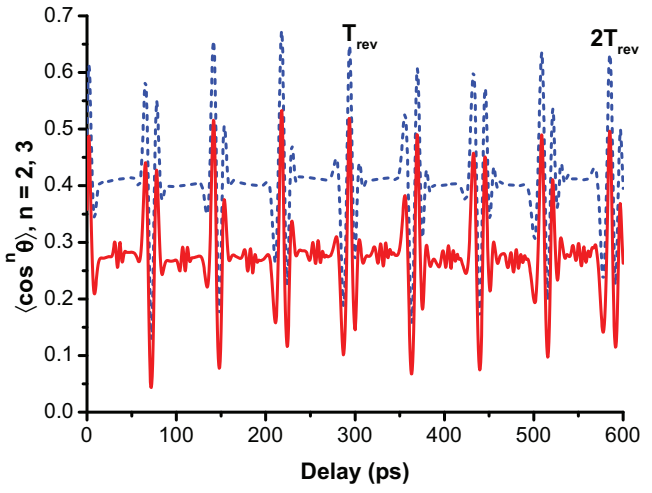

FIG. 4. (Color online) Calculated ensemble averages of $\cos^{2n}\theta$ for $n = 1$ (blue, dashed line) and $n = 2$ (red, solid line) for Ar_2. The time interval up to the second revival of the alignment is shown. $\langle\cos^4\theta\rangle(t)$ clearly shows a $T_{rev}/8$ revival structure. Deviations from a strictly periodic revival structure (period T_{rev}) have their origin in the centrifugal distortion of the Ar_2 dimer due to the rotation.

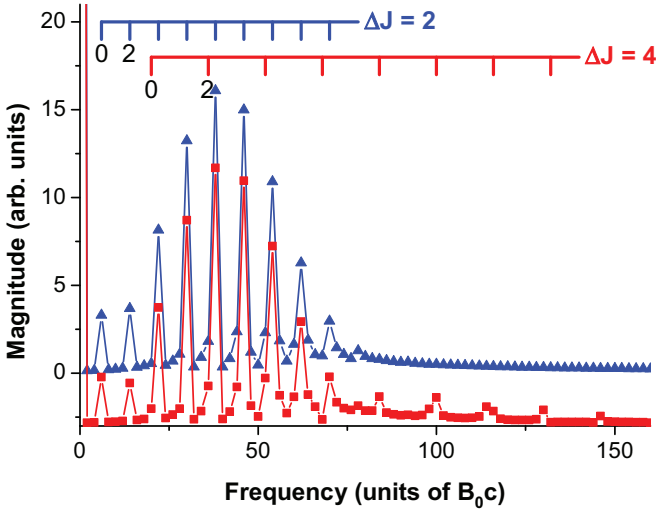

FIG. 5. (Color online) Amplitude (magnitude) of the Fourier transform of the temporal evolution of the ensemble averages $\cos^{2n}\theta$ for $n = 1$ (blue, triangles) and $n = 2$ (red, squares) for Ar_2 (see Fig. 4). Only the time interval $[0, T_{rev}]$ with $T_{rev} = 289.5$ ps has been transformed. The Fourier transform of $\langle\cos^4\theta\rangle(t)$ is shown vertically offset. The markers on top of the Fourier spectra group the spectral lines according to the order ($|J' - J| = \Delta J = 2, 4$) of the coherence they represent. The first two lines in each group are labeled by the rotational quantum numbers of the lower of the two rotational states that are involved in the respective coherence.

are found at $t_n = nT_{rev}/4$ with $n = 1,2,....$ This behavior is similar to the predominant revival structures found in the cut through $\tilde{\rho}(\theta,t)$ at $\theta = 0^\circ$ [Fig. 3(a)]. The function $\langle\cos^2\theta\rangle(t)$ just maps the lowest order coherence present in $\tilde{\rho}(\theta,t)$, namely, that with $\Delta J = 2$. This coherence is easily identified in the Fourier transform of $\langle\cos^2\theta\rangle(t)$ in Fig. 5 (blue triangles). The regular spacing between the lines found in the latter analysis coincides with the eighth harmonic of the rotational frequency in Ar_2. Proceeding from the $\cos^2$ term to $\langle\cos^4\theta\rangle(t)$ (Fig. 4, red solid line), we again identify the partial revivals of the alignment at $t_n = nT_{rev}/4$ ($n = 1,2,...$) as prevalent structures. Additionally, however, regular smaller structures are found at $t_n = (2n+1)T_{rev}/8$ with $n = 1,2,....$ These secondary revivals correspond to $\Delta J = 4$ coherences present in $\tilde{\rho}(\theta,t)$. They also reveal themselves in the Fourier transform of $\langle\cos^4\theta\rangle(t)$ in Fig. 5 (red rectangles). Two groups of lines with regular spacings $\Delta J = 2$ and $\Delta J = 4$ appear here. The $\Delta J = 4$ group of lines is isolated only at large frequencies where the $\Delta J = 2$ group of lines has negligible intensity (see Fig. 5). Similar to the relation between the $\Delta J = 2$ lines in the Fourier transform spectrum of $\langle\cos^2\theta\rangle(t)$ (Fig. 5, blue triangles) and the density matrix elements $\rho_{J+2,M;J,M}(t)$, those with $\Delta J = 4$ in Fig. 5 are related to $\rho_{J+4,M;J,M}(t)$.

The higher order $\Delta J > 2$ coherences present in $\tilde{\rho}(\theta,t)$ predominantly influence, e.g., the cut through $\tilde{\rho}(\theta,t)$ at $\theta = 54^\circ$ [Fig. 3(b)]. These coherences are much better revealed by using the ensemble averages of the even Legendre polynomials $P_{2n}(\cos\theta)$ rather than the averages of $\cos^{2n}\theta$. The ensemble average $\langle P_2(\cos\theta)\rangle(t)$ features similar structures as $\langle\cos^2\theta\rangle(t)$ [Fig. 4(a)]. However, $\langle P_{2n}(\cos\theta)\rangle(t)$ specifically emphasizes $\Delta J = 2n$ coherences. A comparison of the two examples

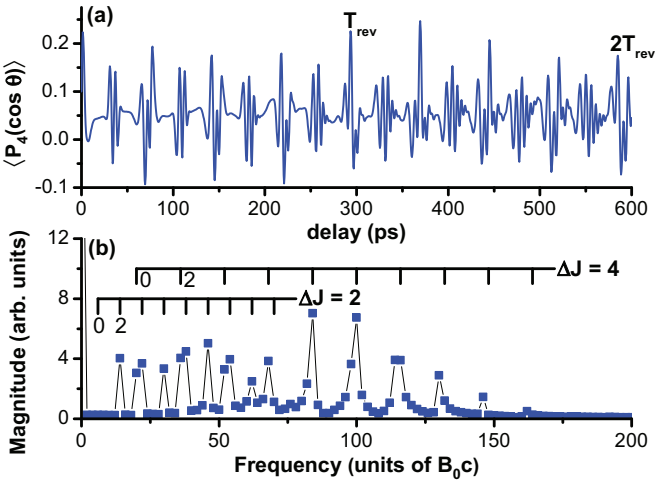

FIG. 6. (Color online) (a) Temporal evolution of the ensemble average of the Legendre polynomial $P_4(\cos\theta)$ for a time interval reaching up to $2T_{\rm rev}$. The obvious deviation of the revival structures from periodicity with $T_{\rm rev}$ is caused by centrifugal distortion of the Ar_2 dimer. (b) Amplitude of the Fourier transform of $\langle P_4(\cos\theta)\rangle(t)$ using the time interval $[0, T_{\rm rev}]$. Similar to Fig. 5, the lines in the spectrum are grouped according to the order ($|J' - J| = \Delta J = 2, 4$) of the coherence that they are representing.

$\langle\cos^{2n}\theta\rangle(t)$ (Fig. 4, red, solid line) and $\langle P_{2n}(\cos\theta)\rangle(t)$ [Fig. 6(a)] for $n = 2$ clearly shows this tendency. In contrast to $\langle\cos^4\theta\rangle(t)$, the partial revival structures at $t_n = (2n+1)T_{\rm rev}/8$ ($n = 1,2,...$) show up very prominently in $\langle P_4(\cos\theta)\rangle(t)$. These structures are responsible for the prominent group of lines that is spaced at $\Delta J = 4$ (16 times the rotational frequency) in the Fourier transform spectrum in Fig. 6(b). $\Delta J = 2$ coherences are not eliminated, yet contribute at reduced intensity at low frequencies [Fig. 6(b)]. This situation prevails for the ensemble averages $\langle P_{2n}(\cos\theta)\rangle(t)$ with $n > 2$.

A specific aspect that one notices in the ensemble averages of $\cos^{2n}\theta$, $n = 1,2$, in Fig. 4 and even more pronounced in $\langle P_4(\cos\theta)\rangle(t)$ [Fig. 6(a)] is the fact that the structures are not strictly periodic with $T_{\rm rev}$. This nonperiodicity has its origin in the centrifugal distortion of the dimer, which was incorporated through the rotational constant D in the second term of the free rotation Hamiltonian [Eq. (2)]. The chosen alignment laser pulse energy is strong enough to populate high-J rotational states, where even the small D_0 for Ar_2 gives rise to an observable effect in the dimer's rotational motion. For the parameters chosen in the calculation, the population

$$w(J) = \sum_{M=-J}^{J} \rho_{J,M;J,M}$$

of the rotational states is shown in Fig. 7. This population does not exhibit a temporal dependence for $t > \tau$. The red dots represent the thermal distribution existing prior to arrival of the alignment pulse and the blue squares the distribution after the pulse. A significant shift in this distribution towards higher rotational states is found for the dimensionless alignment parameter $a = 11.0$ used in the calculation at an initial ensemble temperature of $T = 2.5$ K. This resulting population

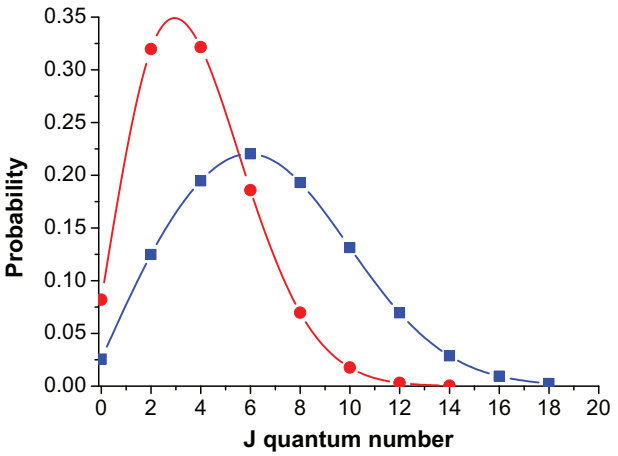

FIG. 7. (Color online) Initial population of the Ar_2 rotational levels J before the alignment laser pulse arrives (red dots) and after the pulse passed (blue squares). The initial temperature of the ensemble of dimers was assumed to be 2.5 K.

distribution cannot be inferred from the time dependence of $\tilde{\rho}(\theta,t)$.

III. EXPERIMENT

A schematic view of the experimental setup is shown in Fig. 8. An amplified Ti:sapphire laser beam (800 nm center wavelength, 25 fs pulse width, 1 mJ pulse energy, 3 kHz pulse repetition rate) was split into an alignment and a probe beam by a mirror with a central hole, the diameter of which was suitably chosen to transmit ≈0.3 mJ of the pulse energy. This part of the beam served as the alignment beam. After passing the mirror, the alignment beam pulses were stretched to a pulse width of ≈1.4 ps (full width at half maximum, FWHM) using two glass blocks consisting of 75 mm of Schott LF5 followed by 30 mm of SF10 glass. We convinced ourselves that this combination does not lead to excessive nonlinear distortions while providing a group-delay dispersion as high as possible. The resulting pulse duration is still short compared to the time scale of rotation of the dimers in order to allow for their impulsive alignment, yet it was sufficiently long to avoid significant multiphoton ionization of the dimers at the elevated pulse energy. The parameters for the alignment beam are close to the optimum value for the nonadiabatic alignment of noble-gas dimers; i.e., an even higher pulse energy would

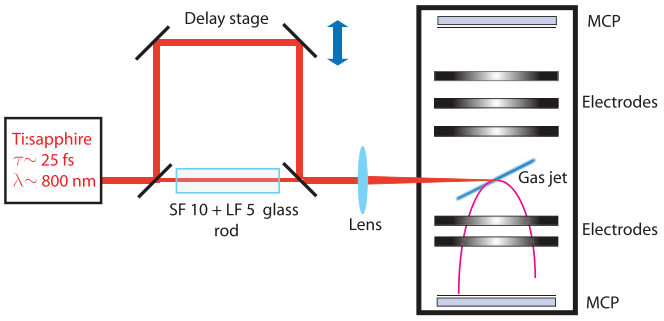

FIG. 8. (Color online) Schematic view of the experimental setup.

lead to the onset of multiphoton ionization whereas a much longer pulse width would result in the alignment being no more strictly nonadiabatic. We note that in the nonadiabatic regime, a reduction of the pulse width at a constant pulse energy does not lead to a higher alignment. The achievable alignment is governed only by the integral over the full pulse width of the square of the electric field strength and not by the instantaneous light intensity [cf. Eq. (6)].

The part of the beam reflected by the drilled mirror (up to 75 μJ of pulse energy) was sent to a variable delay line and served to probe the temporal evolution of the dimer alignment through strong-field double ionization (see Refs. [22,23]). The delay line allowed for a maximum delay of +1.2 ns relative to the aligning laser pulses. Both beams were then recombined on a second mirror with a central hole and sent to the experiment. The beam polarizations were linear and parallel to each other.

Noble-gas dimers were formed by supersonic expansion of the respective noble gas through a nozzle with a diameter of 20 μm. The nozzle temperature and backing pressure were individually set for each gas sample in order to minimize the final beam temperature and optimize the dimer concentration in the beam while keeping larger cluster formation at a minimum. A typical noble-gas dimer concentration of $[Ng_2]/[Ng] \approx 1\%$ was reached in the experiments. After passing through a skimmer, the beam was collimated by a slit aperture, which limited the dimer beam width along the propagation direction of the laser beam to ≈100 μm.

The collinear propagating aligning and probe laser beams intersected the dimer beam at right angles in a cold target recoil ion momentum spectrometer (COLTRIMS) [24] after having been focused by a spherical mirror with 150 mm focal length. The intensities of the aligning and probe beams in the focal spot were $\approx 1 \times 10^{13}$ W/cm^2 and $\approx 3 \times 10^{14}$ W/cm^2, respectively. More details of this setup can be found elsewhere [22,25]. Due to its larger diameter, the probe laser beam focal spot diameter was smaller than that of the alignment beam, therefore only probing the central part of the aligned dimer ensemble, i.e., the very part that interacted with the highest aligning beam fluence. Following double ionization by the probe laser pulse, the dimer ion Coulomb explodes with a specific kinetic energy release (KER) corresponding to the Coulomb repulsion energy at the equilibrium internuclear separation of the dimer, e.g., 3.85 eV for the case of Ar_2) [22,23]. Consequently, in comparison to the rotation of the dimer, the dissociation process is rapid, thus allowing the retrieval of the direction that the internuclear axis was pointing at in the instant of ionization.

The Coulomb explosion channel is identified in the data analysis by selecting atomic ion pairs with zero sum-momentum and the matching KER [22]. For each delay t of the probe pulse relative to the aligning pulse, these ion pairs are used to determine the ion angular distribution $d(\theta,\varphi,t)$ in the Coulomb explosion channel with respect to the common polarization axis of the aligning and probing laser pulses. Here θ is the polar angle with respect to this direction. The axial symmetry of the align/probe configuration makes the distribution independent of the azimuthal angle φ. However, considering ion pairs after double ionization of an unaligned ensemble of dimers, we find that their angular distribution already strongly depends on the polar angle θ [22]. The quantity $d(\theta,t)$ (φ being omitted from here on) therefore encodes the direction that the internuclear axis of the dimer is pointing to at delay time t before double ionization. While the dimer alignment cannot immediately be seen from these measurements, it is, however, readily extracted from $d(\theta,t)$ by recording the corresponding distribution $d_u(\theta)$ for an unaligned ensemble of dimers and then calculating the ratio

$$r(\theta,t) = d(\theta,t)/d_u(\theta) \tag{12}$$

point by point for any given delay time t and polar angle θ. The resulting ratio r is directly proportional to $\tilde{\rho}(\theta,t)$ [Eq. (9)], i.e., the probability density for finding the internuclear axis of the dimer aligned with a polar angle θ with respect to the common direction of polarization of the align/probe pulse pair at time t after the aligning laser pulse and prior to double ionization.

IV. RESULTS AND DISCUSSION

A. The Ar_2 dimer

Figure 9 shows the measured $r(\theta,t)$ [Eq. (12)] as a function of the pump-probe delay for one full revival period of the Ar_2 dimer. The data are a faithful image of $\tilde{\rho}(\theta,t)$ for all θ in the interval $[0,\pi]$ except a small angular range of $\pm 0.1\pi$ around $\pi/2$. Apart from the predominant structures, with alignment revivals appearing at integer multiples of $T_{rev}/4 = 74.9$ ps, much finer details are clearly identifiable in Fig. 10 and correspond to higher order coherences in $\tilde{\rho}(\theta,t)$, i.e., in the rotational motion. For clarity, we restricted ourselves to showing the first 75 ps of the evolution in the latter figure.

From this data, all observables that characterize the alignment of the dimers are extracted, specifically the ensemble averages of the Legendre polynomials $P_{2n}(\cos\theta)$. The ensemble average $\langle\cos^2\theta\rangle$, which is closely related to $\langle P_2(\cos\theta)\rangle$, is shown in Fig. 11(a) as a solid black line. This quantity serves as the commonly used observable for characterization of the net alignment of molecules. We measure a peak alignment $\langle\cos^2\theta\rangle = 0.64$, which is reached exactly at the first half revival ($T_{rev}/2$). The contributions of higher order coherences are extracted by computing the ensemble averages of the

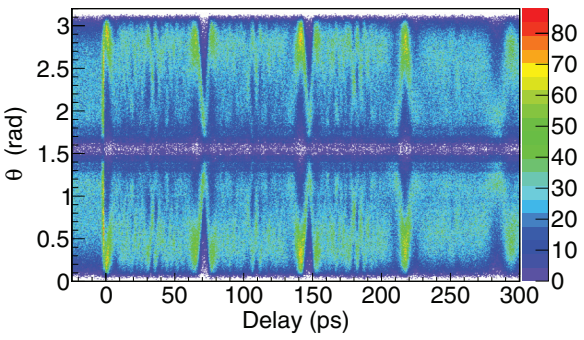

FIG. 9. (Color online) Temporal evolution of the measured $\tilde{\rho}(\theta,t)$ that represents the probability density to find the internuclear axis of Ar_2 aligned with polar angles θ with respect to the axis of polarization of the aligning laser pulse. $t = 0$ represents the instant in time where the ionization laser pulse is synchronous with the aligning laser pulse. The time interval encompassing the first full revival of the alignment at $t = T_{rev} = 289.5$ ps is shown.

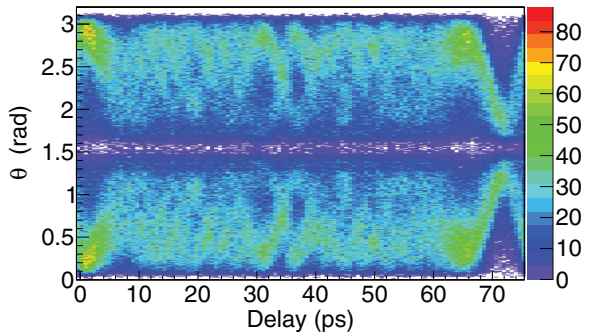

FIG. 10. (Color online) Detailed view of Fig. 9 showing the first 75 ps of the temporal evolution of the alignment.

Legendre polynomials $\langle P_{2n}(\cos\theta)\rangle$ with $n > 1$. Figure 11(b) shows $\langle P_4(\cos\theta)\rangle$ as a black solid line. This observable clearly reveals additional fractional revivals at integer multiples of $T_{\rm rev}/8$, which are not present in $\langle\cos^2\theta\rangle$ and $\langle P_2(\cos\theta)\rangle$. These structures originate from coherences between rotational states with a spacing of $\Delta J = 4$. The temporal evolution of $\langle P_6(\cos\theta)\rangle$ is shown in Fig. 11(c). It reveals even more details of the induced rotational motion than $\langle P_4(\cos\theta)\rangle$ does. We determined the temporal evolution of the ensemble averages $\langle P_{2n}(\cos\theta)\rangle$ up to $n = 4$. Their respective Fourier transforms $\mathcal{F}[\langle P_{2n}(\cos\theta)\rangle]$ or more precisely $|\mathcal{F}[\langle P_{2n}(\cos\theta)\rangle]|$ are shown in Fig. 12. The Fourier transforms $|\mathcal{F}[\langle P_{2n}(\cos\theta)\rangle]|$ are best suited to reveal the higher order coherences in the temporal evolution of the induced alignment, specifically those for rotational states with high angular momentum J. The frequency on the horizontal axes in the Fourier transform spectra is given in multiples of B_0c, with B_0 being the rotational constant of Ar_2 in the vibrational ground state. The Fourier transform $|\mathcal{F}(\langle\cos^2\theta\rangle)|$ [Fig. 12(a)] exclusively shows lines at frequencies that correspond to coherences

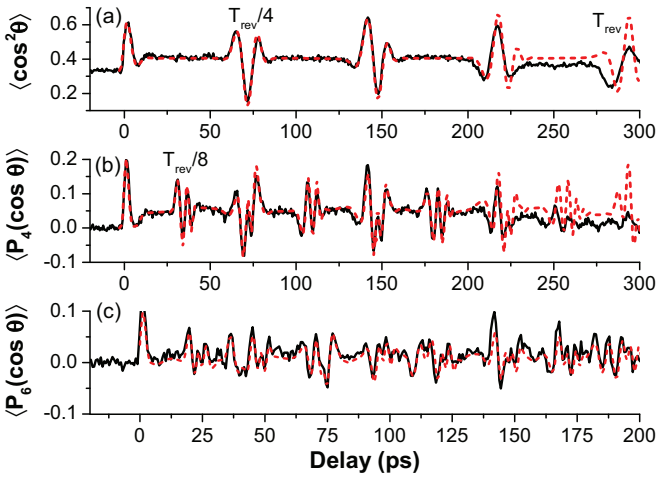

FIG. 11. (Color online) Ar_2: Time dependence of the ensemble averages of $\langle\cos^2\theta\rangle$ (a), $\langle P_4(\cos\theta)\rangle$ (b), and $\langle P_6(\cos\theta)\rangle$ (c) (solid black lines) determined from experimental data. Red dashed lines show the corresponding calculated time dependencies of $\langle\cos^2\theta\rangle$ and $\langle P_{2n}(\cos\theta)\rangle$, respectively, using a kick parameter $a = 11.0$, an initial ensemble temperature of 2.5 K, and an alignment laser pulse width of 1.4 ps FWHM.

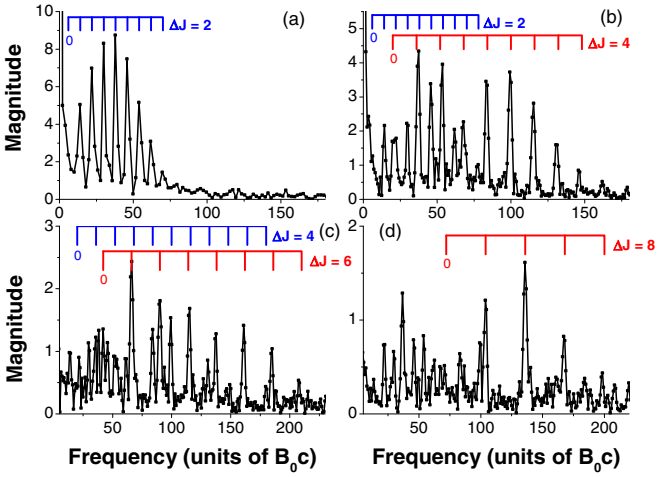

FIG. 12. (Color online) Ar_2: Amplitudes of the Fourier transforms of the experimentally determined ensemble averages $\langle\cos^2\theta\rangle$ (a) and $\langle P_{2n}(\cos\theta)\rangle$ for $n = 2$–4 [(b) through (d), respectively]. Coherences present in the temporal evolution of the alignment appear as lines in these spectra. Lines are grouped according to the order ΔJ of the respective coherence. The lowest frequency line of each group is identified by the rotational quantum number J of the lower one of the two rotational states that is involved in the respective coherence. Within each group, J increases in steps of two from one line to the other.

between rotational states with $\Delta J = 2$. This line structure is theoretically expected [see Eqs. (9), (10)]. The spacing between the individual lines in this Fourier spectrum is found to be equal to $\Delta\nu = 8nB_0c$, with $n = 1$ in this case (see below). The markers on top of the spectrum identify the lines with the respective rotational quantum number J of the lower rotational state that is involved in the corresponding coherence of the rotational motion ($\Delta J = J' - J = 2$). These lowest order coherences can be followed up to a rotational state $J = 16$. This means that $J' = J + 2 = 18$ corresponds to the highest rotational state which got significantly populated by the aligning laser pulse. This finding is confirmed by the calculated population distribution after the aligning laser pulse passed, which is shown in Fig. 7. The calculation used parameters adapted to the experimental situation. The height distribution of the lines in the Fourier transform spectrum resembles the population distribution of the rotational states in Fig. 7. However, one has to keep in mind that Figs. 7 and 12(a) represent completely different elements of the density matrix. The population distribution in Fig. 7 represents stationary diagonal matrix elements, i.e., after the aligning laser pulse has already passed. In contrast, the Fourier transform spectrum $|\mathcal{F}(\langle\cos^2\theta\rangle)|$ in Fig. 12(a) represents time-dependent off-diagonal density matrix elements $\rho_{J,M;J',M}(t)$ with $|J - J'| = 2$.

The Fourier transform $|\mathcal{F}[\langle P_4(\cos\theta)\rangle]|$ of $P_4(\cos\theta)(t)$ [Fig. 12(b)] additionally contains lines with a frequency spacing twice that of $|\mathcal{F}[\langle P_2(\cos\theta)\rangle]|$ [Fig. 12(a)], corresponding to coherences with $\Delta J = 4$. Contributions from lower order coherences are not completely suppressed although the suppression is much better than one would expect from the ensemble average $\langle\cos^4\theta\rangle$. Similarly, $\Delta J = 6$ and $\Delta J = 8$

coherences are unambiguously identifiable in the Fourier spectra $|\mathcal{F}[\langle P_6(\cos\theta)\rangle]|$ and $|\mathcal{F}[\langle P_8(\cos\theta)\rangle]|$, respectively [Figs. 12(c), 12(d)]. The markers on top of the lines have been inserted in all of the Fourier spectra in Fig. 12, and these markers are grouped according to the order ΔJ of the coherence they represent. Additionally, within each group, the quantum number of the lower rotational state is indicated that contributes to the lowest frequency line. The frequencies of the lines that represent the respective highest order coherence ($\Delta J = 2n$) in the Fourier spectra $|\mathcal{F}[\langle P_{2n}(\cos\theta)\rangle]|$ can be shown to be given by

$$\omega(J, J+2n) = E_{J+2n} - E_J = 2\pi B_0 c[(J+2n)(J+2n+1) - J(J+1)]. \quad (13)$$

It should be pointed out that this treatment ignores the centrifugal distortion part in the free rotation Hamiltonian Eq. (2). The positions of the markers shown in Fig. 12 have been determined using relation (13) above. They are seen to be in good agreement with the actually observed frequencies of the lines found in the Fourier spectra. From relation (13) the spacing of the lines within the group of lines representing the respective highest order coherence can be determined. This spacing is given by $\Delta\nu = \Delta\omega/2\pi = 8nB_0c$.

In order to extract more information from the measured alignment traces, we performed calculations based on a numerical solution of the time-dependent Schrödinger equation; see Sec. II. The rotational temperature is assumed to be close to the translational temperature in the gas jet (2.5 K). As a starting point for the calculation, we used the rotational constant $B_0 = 0.05756\ \text{cm}^{-1}$ taken from a recent demonstration of the impulsive alignment of Ar_2 by Wu *et al.* [17]. This value is expected to be close to the actual rotational constant B_0, since in the experiment of Wu *et al.* only a coherent excitation of low-J states was induced by the alignment laser pulse. This means, the alignment revival time T_{rev} used there to determine B_0 can be assumed to be influenced only slightly by centrifugal distortion. We note that for the strong alignment present in our experiment, the population of high-lying rotational states (Fig. 7) leads to a noticeable effect of the centrifugal distortion on the energy of the high-J rotational eigenstates involved in the wave packet and therefore on T_{rev}. It is not possible to retrieve the rotational constant B_0 accurately from a measurement of the full revival time $T_{\text{rev}} = 292.0 \pm 0.5$ ps in Fig. 11(a). This value of T_{rev} would give rise to $B_0 = 0.05712 \pm 0.0001\ \text{cm}^{-1}$, which is significantly smaller than the value provided by Wu *et al.* [17]. It is the centrifugal distortion of Ar_2 that is responsible for the observed difference.

The remaining unknown parameters for the calculation are the polarizability anisotropy $\Delta\alpha$ and the laser pulse fluence that the dimers interacted with. Both quantities together yield the kick parameter a [Eq. (6)], which defines the alignment in the impulsive limit. In principle, knowledge of the fluence enables one to extract the absolute value of $\Delta\alpha$ by fitting calculated data to the experimental ones. However, the exact geometry and the precise degree of overlap between pump and probe pulses is unknown. Therefore, we used different values of the kick parameter a to fit the calculated to the measured data. The kick parameter essentially influences the amplitude of the revivals and the baseline alignment in $\langle P_{2n}(\cos\theta)\rangle(t)$. The fit was done for fixed pulse width τ and shape. At the pulse width used in the experiment, the calculated temporal evolution of $\langle P_{2n}(\cos\theta)\rangle$ after the aligning laser pulse is practically insensitive to τ and to the specific pulse shape. This means, we are actually well in the impulsive limit for initiation of the alignment. Calculations were performed with different values of the rotational constant B_0 and the centrifugal distortion D_0 in order to match the position in time and the precise shape of the revivals. The best fit to the experimental data is shown in Fig. 11 superimposed on these data (red dashed line). It is obtained for $B_0 = 0.0576 \pm 0.0001\ \text{cm}^{-1}$ and $D_0 = (1.2 \pm 0.2) \times 10^{-6}\ \text{cm}^{-1}$, i.e., in good agreement with earlier spectroscopic measurements ($D_0 = 1.22 \times 10^{-6}\ \text{cm}^{-1}$ [21]). The error margins indicate the values of B_0 and D_0 for which a perceptible deviation of the calculation from the experimental data is reached. At delays larger than 200 ps, the difference in the amplitudes of the calculated and measured alignment increases independent of the parameters chosen for the calculation to fit the data, with the fit being based on the time interval up to 200 ps. This difference is caused by a small angular pitch ($\approx 100\ \mu$rad) of the translation stage used to scan the delay between the aligning and probe laser pulses. The pitch leads to a displacement of the probe pulse focal spot with respect to that of the alignment pulse. We can exclude that this decrease is caused by centrifugal distortion since it affected all our measurements in the same way, independent of the dimer species investigated.

The value of the kick parameter a [Eq. (6)] that corresponds to the best fit is found to be $a = 11.0$ for Ar_2. We use the latter value as a starting point to determine relative values for the polarizability anisotropy parameters $\Delta\alpha$ of the other noble-gas dimers Ne_2, Kr_2, and Xe_2. For each dimer species we optimized the respective kick parameter a to fit the measured $\langle P_{2n}(\cos\theta)\rangle(t)$ ($n \leqslant 3$) data. Since the aligning pulse parameters are the same for all measurements, the ratio of the kick parameters for the different dimers equals the ratio of the polarizability anisotropies. Based on the reference value $\Delta\alpha = 0.45\ \text{Å}^3$ for Ar_2 stated in the experimental investigation of Minemoto *et al.* [16], we are now able to determine $\Delta\alpha$ for the other dimers from our experimental data. The values of $\Delta\alpha$ are summarized in Table I.

TABLE I. Polarization anisotropies $\Delta\alpha$ for the noble-gas dimers investigated (in Å^3). The value for Ar_2 from Ref. [16] (second column) is used as a reference value. We determined the anisotropies for the other dimers relative to this value. The theoretical values of Ref. [26] are the polarization anisotropies at the respective equilibrium internuclear separations of the dimers. The experimental values given in the second and last columns are the expectation values of $\Delta\alpha$ in the respective vibrational ground state.

	$\Delta\alpha$ calc.	$\Delta\alpha$ exp. [16]	$\Delta\alpha$ this work
Ne_2	0.022–0.029 [26]		0.026(6)
Ar_2	0.27–0.31 [26]	0.45(13)	0.45 (ref. value, see text)
$^{84}Kr_2$	0.53–0.59 [26]	0.72(13)	0.63(10)
$^{132}Xe_2$	1.27–1.37 [27]	1.23(21)	1.35(20)

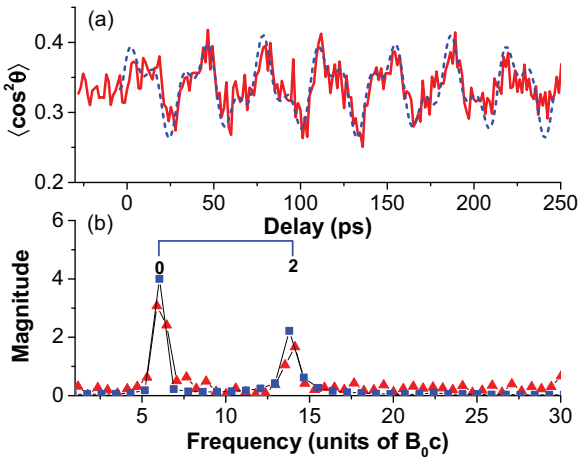

FIG. 13. (Color online) Ne_2: Time dependence of the ensemble average $\langle\cos^2\theta\rangle$ (a) and its Fourier transform (b). (a) Solid red line: experimental data. Dashed blue line: calculated $\langle\cos^2\theta\rangle(t)$ that best fits the experiment. (b) Red triangles: experimental data. Blue squares: Fourier transform of the calculated $\langle\cos^2\theta\rangle(t)$.

B. The Ne_2 dimer

The evolution in time of the experimentally determined ensemble average $\langle\cos^2\theta\rangle(t)$ for Ne_2 is shown in Fig. 13(a) as solid red line. The aligning laser pulse fluence was identical to that used for Ar_2. Since most of the laser output power was used for the alignment, the ionizing pulse was limited in intensity, resulting in a much lower double ionization probability of Ne_2. Therefore, the total number of acquired events is lower than it was in the case of Ar_2, resulting in an inferior statistics. From Fig. 13(a), it is evident that the peak alignment ($\langle\cos^2\theta\rangle = 0.42$) is much lower than for Ar_2. This means, the polarizability anisotropy in Ne_2 is significantly smaller than in Ar_2. The Fourier transform of $\langle\cos^2\theta\rangle(t)$ shown in Fig. 13(b) (red triangles) reveals that only two frequencies significantly contribute to the $\langle\cos^2\theta\rangle(t)$ alignment trace. The two observed lines represent the $\Delta J = 2$ coherences in the evolution in time of the Ne_2 alignment. The presence of only these two lines immediately means that no higher order coherences are present in the temporal evolution of the rotational wave packet. As for the argon dimer the lines in the Fourier spectrum are identified by the corresponding rotational quantum numbers. The spacing of the lines is 37 ± 1 GHz, from which we obtain a rotational constant of $B_0 = 0.154 \pm 0.004$ cm^{-1}. Since only the lowest J rotational states are occupied, any effect of centrifugal distortion on deriving the rotational constant from this line spacing can safely be neglected. Given that the polarizability anisotropy in Ne_2 is significantly smaller than for Ar_2, the presence of higher order coherences in the density matrix, i.e., the rotational wave packet, can in fact not be expected for the alignment pulse parameters employed here.

Figure 13(a) shows a fit (blue dashed line) to the experimental alignment trace based on numerical calculations. Best agreement with the experimental data is obtained for a kick parameter $a = 0.63$. This value amounts to only six percent of the value that was measured for Ar_2. Taking the value of Minemoto *et al.* for Ar_2 as a reference ($\Delta\alpha = 0.45$ Å^3) [16], we obtain a polarizability anisotropy of $\Delta\alpha = 0.026 \pm 0.006$ Å^3 for Ne_2; see Table I. This value is in good agreement with results from calculations ranging from $\Delta\alpha = 0.022$ Å^3 to 0.029 Å^3 obtained with a range of theoretical methods [26]. The Fourier transform of the calculated evolution in time of $\langle\cos^2\theta\rangle(t)$ is shown in Fig. 13(b) (blue squares). It is in similar good agreement with the experimental data as are the calculated and experimentally determined traces of the temporal evolution of the alignment in Fig. 13(a).

C. The Kr_2 dimer

Figure 14(a) shows the temporal evolution of the experimentally determined ensemble average $\langle\cos^2\theta\rangle$ for Kr_2 over a delay interval of ≈1200 ps as a solid red line. The apparent wavy structure of the alignment baseline and fluctuations in the maximum alignment reached in the revivals have their origin in the position-dependent pitch inaccuracies of the translation stage used to delay the Coulomb explosion pulse. Kr gas contains several isotopes that give rise to the formation of dimers with different isotopic constituents. For the data shown in Fig. 14(a), only Coulomb explosion events of $^{84}Kr_2$ have been taken into account as this is the isotope with the highest natural abundance. The ^{84}Kr isotope has zero nuclear spin. Consequently, as for Ar_2, therefore fractional revivals with period $T_{rev}/4$ also appear here. The contribution of higher order coherences to the experimentally determined $\tilde{\rho}(\theta,t)$ is revealed by Fourier transforming the ensemble averages $\langle\cos^2\theta\rangle(t)$ and $\langle P_{2n}(\cos\theta)\rangle(t)$ for $n = 2, 3$. These Fourier transform spectra are shown in Figs. 14(b)–14(d), respectively. Similarly to Ar_2, we find a significant contribution of higher order coherences in the rotational wave packet. These coherences are identified by the markers with the respective lower rotational quantum number indicated on the lines in the Fourier spectra. The spectra indicate that rotational levels up to $J = 26$ become populated in the aligned ensemble.

The retrieval of the polarizability anisotropy $\Delta\alpha$ for $^{84}Kr_2$ was done employing only the part of the experimental data with a pump/probe delay smaller than 200 ps. In this delay range we can be certain to probe the alignment in a focal volume where the fluence of the aligning laser beam is identical to the Ar_2 experiment conducted in the same time interval. By fitting the numerically calculated $\langle\cos^2\theta\rangle(t)$ distribution to the experimental data, we obtain the best fit for a kick parameter of $a = 15.4$, which is 1.4 times the value for Ar_2; see Table I. The rotational constants B_0 and D_0, on the other hand, are determined precisely by fitting the calculated $\langle\cos^2\theta\rangle(t)$ with a reduced kick parameter a [Eq. (6)] to the experimental $\langle\cos^2\theta\rangle(t)$ trace in the range of large pump/probe delays. We find a rotational constant of $B_0 = 0.0244 \pm 0.0001$ cm^{-1}. We also yield an estimate $D_0 = (1.0 \pm 0.4) \times 10^{-7}$ cm^{-1} for the centrifugal distortion. This value best reproduces the details in the structures of the revival oscillations as can be seen in Fig. 15, which shows details of one of the observed revival structures together with two calculated ensemble averages for different D_0.

Yet again taking Ar_2 as a reference, the value of $\Delta\alpha = 0.63$ Å^3 that we get from our experiment is in fair agreement

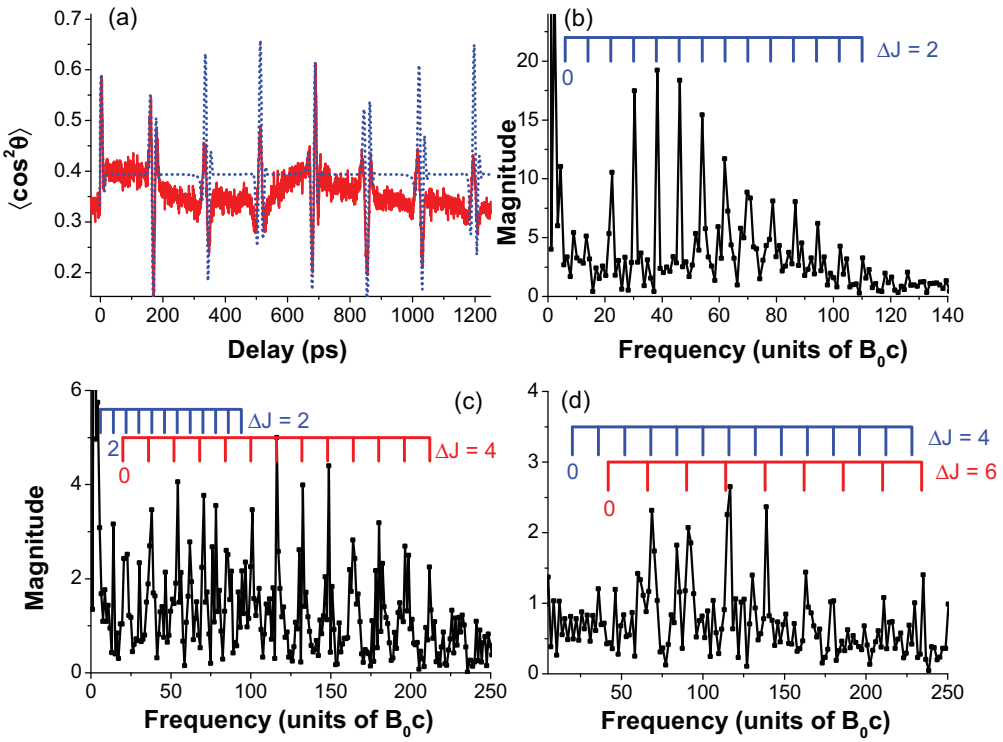

FIG. 14. (Color online) $^{84}Kr_2$: (a) Temporal evolution of the experimentally determined (red, solid line) and of a calculated (blue, dashed line) ensemble average $\langle\cos^2\theta\rangle$. The calculated average was chosen as to best fit the experimental data in the time span up to 200 ps. (b) the Fourier transform of the experimental ensemble average $\langle\cos^2\theta\rangle(t)$. (c), (d) The Fourier transforms of the experimental ensemble averages $\langle P_{2n}(\cos\theta)\rangle$ for $n = 2$ (c), and 3 (d). The grouping of the lines in the Fourier spectra is analogous to that used for Ar_2 (Fig. 12).

with the one measured by Minemoto *et al.*, i.e., $\Delta\alpha = 0.72$ Å^3 [16]. The latter authors used adiabatic alignment of Kr_2 to determine $\Delta\alpha$. Moreover, our result agrees well with theoretical values for $\Delta\alpha$ obtained in Ref. [26]. The resulting polarizability anisotropies in that work range from $\Delta\alpha = 0.53$ Å^3 to $\Delta\alpha = 0.59$ Å^3.

D. The Xe_2 dimer

Similar to krypton, xenon gas is a mixture of even more isotopic constituents. This fact gives rise to a broad distribution of dimers with different isotopic composition. Here we investigate only one of these compositions, namely $^{132}Xe_2$. The temporal evolution of the ensemble average $\langle\cos^2\theta\rangle(t)$ after the aligning laser pulse for this dimer is shown in Fig. 16

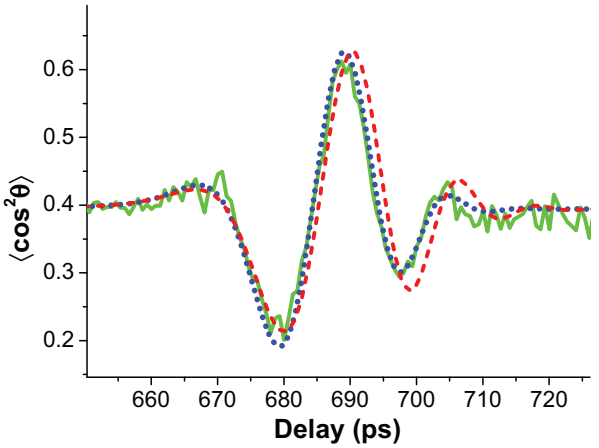

FIG. 15. (Color online) Ensemble average $\langle\cos^2\theta\rangle(t)$ in the neighborhood of the full revival period $T_{rev} = 683.5$ ps for $^{84}Kr_2$. Shown are the experimental data (green solid line) and two fits to the experimental data calculated assuming $D_0 = 1.0 \times 10^{-7}$ cm^{-1} (blue dotted line) and $D_0 = 1.5 \times 10^{-7}$ cm^{-1} (red dashed line).

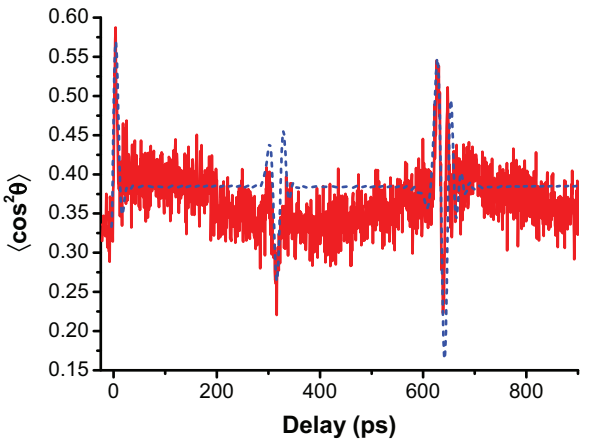

FIG. 16. (Color online) $^{132}Xe_2$: Experimentally determined time dependence of the ensemble average of $\cos^2\theta$ (solid red line). Dashed blue line: calculated $\langle\cos^2\theta\rangle(t)$ using a polarizability anisotropy that best fits the alignment maximum directly following the aligning laser pulse at zero delay.

TABLE II. Rotational constants B_0 and D_0 of the noble-gas dimers in the vibrational ground state as determined from our experiment.

	B_0 (cm^{-1})	D_0 ($10^{-6} cm^{-1}$)
Ne_2	0.154(4)	
Ar_2	0.0576(1)	1.2(2)
$^{84}Kr_2$	0.0244(1)	0.10(4)
$^{132}Xe_2$	0.01315(15)	0.02(1)

as a red solid line. Compared to the experiments in argon and krypton, the signal-to-noise ratio appears worse, which is not a surprise given the large number of different Xe isotopes in the gas jet and the low high-mass-ion detection efficiency of the microchannel plates that were used for ion detection. Consequently, we did not achieve a satisfactory signal-to-noise level that would allow sensible analysis of higher order coherences of the density matrix for the aligned xenon ensemble. Therefore, we restrict ourselves to an analysis of $\langle\cos^2\theta\rangle(t)$. By fitting the numerically calculated $\langle\cos^2\theta\rangle(t)$ to the first alignment maximum directly following the aligning laser pulse, we estimate a polarizability anisotropy that is three times higher than the value of Ar_2. This analysis results in a $\Delta\alpha = 1.35 \pm 0.2$ Å^3 for the polarizability anisotropy of $^{132}Xe_2$, which is again based on the reference value of Ar_2 given in [16]. Moreover, this value is in good agreement with calculations from Maroulis *et al.* [27] ($\Delta\alpha = 1.27$–1.37 Å^3). The best fit to the experimental data for large probe delay times is found for a rotational constant $B_0 = 0.01315 \pm 0.00015$ cm^{-1}. Reproduction of the alignment ringing directly following the first half revival at $T_{rev}/2 = 635.1$ ps necessitates the assumption of a centrifugal distortion of $D_0 = (2 \pm 1) \times 10^{-8}$ cm^{-1} for the $^{132}Xe_2$ isotope.

The measured values for the rotational constants B_0 and D_0 in the vibrational ground state of the dimers are summarized in Table II. The constant D_0 governs the centrifugal distortion of the dimer with increasing rotational quantum number to lowest order. Apart from Ne_2 where it was not possible to determine D_0, we see a general trend of D_0 dropping from Ar_2 to $^{132}Xe_2$ by nearly two orders of magnitude. This finding is corroborated by the expected increasing binding strength of the van der Waals potential. The polarizability anisotropy $\Delta\alpha$ (Table I) increases from Ne_2 to $^{132}Xe_2$, with a marked step between Ne_2 and Ar_2. The small polarizability anisotropy for Ne_2 is caused by the intrinsically small polarizability of the Ne atoms.

V. CONCLUSIONS

We presented detailed experimental and theoretical results on laser-induced alignment of noble-gas dimers in the nonadiabatic regime. By using alignment laser pulses stretched to picosecond pulse duration we have been able to apply a high fluence to the dimers, thus achieving a considerably high alignment while still being in the impulsive regime with the laser pulses. We were able to extract values of the rotational constants B_0 and D_0 from the measured data together with estimates for the polarizability anisotropies $\Delta\alpha$ for Ne_2 to Xe_2 by comparing the experimental data to calculations. We highlighted the role of higher order coherences in the rotational wave packet that is launched by the aligning laser pulse. These coherences are closely related to the time dependence of the off-diagonal elements of the density matrix which characterizes the aligned ensemble of molecules. The coherences, specifically the higher order ones, manifest themselves in the temporal evolution of the ensemble averages of Legendre polynomials $P_{2n}(\cos\theta)$ of even order. A Legendre polynomial $P_{2n}(\cos\theta)$ of order $2n$ can reveal coherences up to the order $\Delta J = 2n$ in the rotational wave packet, with the highest order being most prominent. Our results show that these coherences are best identifiable in the Fourier transforms of these time-dependent ensemble averages. The lines appearing in the Fourier spectra are closely related to the off-diagonal elements $\rho_{J',M;J,M}(t)$ with $|J' - J| = \Delta J \geqslant 2$ of the density matrix. For any statistical ensemble of molecules that initially differs from a pure state ensemble, just the higher order coherences, i.e., the far-off-diagonal elements of the density matrix, are essential to characterize the temporal evolution of the wave packet launched by an aligning laser pulse completely. In this case these higher order coherences ($\Delta J > 2$) and consequently the corresponding off-diagonal density matrix elements cannot be inferred from the lowest order one with $|J' - J| = \Delta J = 2$ and the population distribution over the rotational states of the aligned ensemble. All off-diagonal density matrix elements are independent quantities which have to be determined individually for a complete characterization of the rotational wave packet. An inference, as it is mentioned above, is only possible for an ensemble in a pure initial state.

The most complete direct access to the high-order coherences and therefore to the far-off-diagonal density matrix elements is possible by Coulomb exploding or dissociating the aligned molecules. In our case Coulomb explosion imaging revealed the complete view on all the details of the temporal evolution of the rotational wave packet launched by an impulsive aligning laser pulse. Our results show that with this method unavailable for a specific situation it is necessary to employ other, possibly more demanding methods which are capable of giving access to all the high-order coherences in the rotational wave packet. Only then a complete characterization of the induced rotational motion is possible.

ACKNOWLEDGMENT

We gratefully acknowledge funding by the Deutsche Forschungsgemeinschaft (DFG).

[1] H. Stapelfeldt and T. Seideman, Rev. Mod. Phys. **75**, 543 (2003).

[2] C. Vallance, Phys. Chem. Chem. Phys. **13**, 14427 (2011).

[3] B. Friedrich and D. Herschbach, Phys. Rev. Lett. **74**, 4623 (1995).

[4] T. Seideman, J. Chem. Phys. **103**, 7887 (1995).

[5] V. Kumarappan, L. Holmegaard, C. Martiny, C. B. Madsen, T. K. Kjeldsen, S. S. Viftrup, L. B. Madsen, and H. Stapelfeldt, Phys. Rev. Lett. **100**, 093006 (2008).
[6] F. Kelkensberg, A. Rouzée, W. Siu, G. Gademann, P. Johnsson, M. Lucchini, R. R. Lucchese, and M. J. J. Vrakking, Phys. Rev. A **84**, 051404 (2011).
[7] O. Smirnova, Y. Mairesse, S. Patchkovskii, N. Dudovich, D. Villeneuve, P. Corkum, and M. Y. Ivanov, Nature (London) **460**, 972 (2009).
[8] O. Smirnova, S. Patchkovskii, Y. Mairesse, N. Dudovich, and M. Y. Ivanov, Proc. Natl. Acad. Sci. USA **106**, 16556 (2009).
[9] S. Haessler, J. Caillat, W. Boutu, C. Giovanetti-Teixeira, T. Ruchon, T. Auguste, Z. Diveki, P. Breger, A. Maquet, B. Carré, R. Taïeb, and P. Salières, Nat. Phys. **6**, 200 (2010).
[10] D. Shreenivas, A. Lee, N. Walter, D. Sampayo, S. Bennett, and T. Seideman, J. Phys. Chem. A **114**, 5674 (2010).
[11] S. Ramakrishna and T. Seideman, Phys. Rev. A **87**, 023411 (2013).
[12] F. Rosca-Pruna and M. J. J. Vrakking, Phys. Rev. Lett. **87**, 153902 (2001).
[13] P. W. Dooley, I. V. Litvinyuk, K. F. Lee, D. M. Rayner, M. Spanner, D. M. Villeneuve, and P. B. Corkum, Phys. Rev. A **68**, 023406 (2003).
[14] T. Seideman and E. Hamilton, Adv. At. Mol. Opt. Phys. **52**, 289 (2005).
[15] S. Minemoto, H. Tanji, and H. Sakai, J. Chem. Phys. **119**, 7737 (2003).
[16] S. Minemoto and H. Sakai, J. Chem. Phys. **134**, 214305 (2011).
[17] J. Wu, A. Vredenborg, B. Ulrich, L. P. H. Schmidt, M. Meckel, S. Voss, H. Sann, H. Kim, T. Jahnke, and R. Dörner, Phys. Rev. A **83**, 061403 (2011).
[18] J. Ortigoso, M. Rodríguez, M. Gupta, and B. Friedrich, J. Chem. Phys. **110**, 3870 (1999).
[19] H. P. Godfried and I. F. Silvera, Phys. Rev. A **27**, 3008 (1983).
[20] H. P. Godfried and I. F. Silvera, Phys. Rev. Lett. **48**, 1337 (1982).
[21] P. R. Herman, P. E. LaRocque, and B. P. Stoicheff, J. Chem. Phys. **89**, 4535 (1988).
[22] B. Manschwetus, H. Rottke, G. Steinmeyer, L. Foucar, A. Czasch, H. Schmidt-Böcking, and W. Sandner, Phys. Rev. A **82**, 013413 (2010).
[23] B. Ulrich, A. Vredenborg, A. Malakzadeh, M. Meckel, K. Cole, M. Smolarski, Z. Chang, T. Jahnke, and R. Dörner, Phys. Rev. A **82**, 013412 (2010).
[24] J. Ullrich, R. Moshammer, A. Dorn, R. Dörner, L. P. H. Schmidt, and H. Schmidt-Böcking, Rep. Prog. Phys. **66**, 1463 (2003).
[25] Z. Ansari, M. Böttcher, B. Manschwetus, H. Rottke, W. Sandner, A. Verhoef, M. Lezius, G. G. Paulus, A. Saenz, and D. B. Milošević, New J. Phys. **10**, 093027 (2008).
[26] G. Maroulis, J. Phys. Chem. A **104**, 4772 (2000).
[27] G. Maroulis, A. Haskopoulos, and D. Xenides, Chem. Phys. Lett. **396**, 59 (2004).